THE ASTROPHYSICAL JOURNAL, 425:695–706, 1994 April 20

THE MASSIVE MOLECULAR OUTFLOW FROM CRL 2136 IRS 1

JOEL H. KASTNER,[1] DAVID A. WEINTRAUB,[2] RONALD L. SNELL,[3] G. SANDELL,[4] C. ASPIN,[4]
D. H. HUGHES,[5] AND F. BAAS[4]

Received 1993 August 2; accepted 1993 October 26

ABSTRACT

Maps of rotational CO emission toward the star-formation region CRL 2136 reveal an arcminute-scale bipolar outflow that appears to be driven by the massive young stellar object IRS 1. The projected outflow axis is roughly perpendicular to the disk plane previously inferred from near-infrared images and polarization maps. High-velocity wings are present in both ^{12}CO and ^{13}CO spectra, suggesting the ^{12}CO optical depths in the outflowing gas are large; we estimate the high-velocity gas contains $\sim 50\ M_\odot$, making this molecular outflow one of the more massive known. We find that the region within $\sim 1'$ of CRL 2136 constitutes a significant concentration of the molecular mass in the ambient cloud.

Submillimeter photometry and mapping shows that CRL 2136 is a strong, extended source of continuum emission. The emission likely arises with grains heated to 40–60 K by IRS 1. Comparison of the estimated thermal dust mass ($\sim 1\ M_\odot$ within $\sim 8''$ of IRS 1), the mass in high-velocity gas, and the scattering dust mass we derived previously suggests that the gas-to-dust mass ratio in the outflow is between ~ 10 and ~ 100, where the value depends on what proportion of the submillimeter emission originates with dust in the ambient cloud and/or circumstellar disk.

The apparent extreme youth of IRS 1 compared with the dynamical age of the outflow, and the tremendous mass of swept-up molecular material, suggests the outflow began early in the formation of the young stellar object and implies the outflow cannot be radiatively driven. We present evidence that infall toward IRS 1 is ongoing; transfer of angular momentum from this infalling material may drive the outflow.

Subject headings: dust, extinction — ISM: individual (CRL 2136) — ISM: jets and outflows — ISM: molecules — stars: formation

1. INTRODUCTION

The intense mid- and far-infrared source CRL 2136 = IRAS 18196−1331 is associated with a region of star formation in a dense molecular cloud (Kastner, Weintraub, & Aspin 1992, hereafter Paper I, and references therein). The kinematic distance to this region is ~ 2 kpc (Paper I). Polarimetric near-infrared images of CRL 2136 (Paper I; Minchin et al. 1991) reveal a complex reflection nebula (the Juggler nebula) that is $\sim 1'$ in length and is illuminated by the infrared point source IRS 1 ($\alpha_{1950} = 18^h19^m36^s.7$, $\delta_{1950} = -13°31'47''(\pm 2'')$; Paper I). In Paper I, we suggested that the Juggler nebula outlines cavities created by an outflow or outflows from IRS 1, and that IRS 1 is likely a massive ($\gtrsim 10\ M_\odot$) young stellar object (YSO). The pattern of near-infrared polarization within $\sim 5''$ of IRS 1—a region of the Juggler nebula where the polarization position angles are elliptically rather than circularly symmetric—indicates the presence of an optically thick circumstellar disk or torus oriented at position angle $\sim 45°$ (Paper I; Minchin et al. 1991). This orientation suggests that, should CRL 2136 possess a molecular outflow, the outflow axis should lie near position angle $\sim 135°$; however, there appears to be no previous identification of a molecular outflow with CRL 2136. Given the ubiquity of the outflow phase in early stages of stellar evolution (e.g., Fukui et al. 1989), the lack of an outflow from such a massive, luminous YSO would be significant. On the other hand, its omission from existing lists of YSO outflows might be due to its location near the Galactic plane toward a region of intense background CO emission (Galactic coordinates $l^{II} = 17.^\circ63$, $b^{II} = 0.^\circ16$).

To determine whether CRL 2136 possesses an outflow, and to better understand the relationship between CRL 2136 and the dense cloud out of which it has formed, we used three radio telescopes to map millimeter-wave molecular emission and submillimeter continuum emission in a region centred on IRS 1. We also obtained a large-field near-infrared image and millimeter and submillimeter photometry of the CRL 2136 region. The molecular line observations reveal a bipolar outflow that is among the largest and most massive YSO outflows known in the galaxy. Furthermore, the outflow appears to be oriented perpendicular to the disk plane, as inferred from the near-infrared polarimetry. Observations are described in § 2. In § 3, we present maps of the source and its spectral energy distribution from 1 μm to 2 mm. From the CO and submillimeter data, we estimate molecular excitation temperatures and gas and dust masses in the outflow and the host molecular cloud. Section 4 contains a discussion and § 5 contains conclusions.

2. OBSERVATIONS

2.1. *FCRAO/QUARRY*

Spectral line maps of the CRL 2136 region were obtained at the $J = 1 \rightarrow 0$ transitions of ^{12}CO (115.2712 GHz) and ^{13}CO

[1] MIT Haystack Observatory, Route 40, Westford, MA 01886. Postal address: MIT Center for Space Research, 37-667a, Cambridge, MA 02139. E-mail: jhk@juggler.mit.edu.
[2] Department of Physics and Astronomy, Vanderbilt University, Nashville, TN 37235.
[3] Five College Radio Astronomy Observatory, University of Massachusetts, Amherst, MA 01003.
[4] Joint Astronomy Centre, 600 North Aohoku Place, University Park, Hilo, HI 96720.
[5] Astrophysics, Department of Physics, University of Oxford, Keble Road, Oxford OX1 3RH, UK.

TABLE 1

LOG OF LINE OBSERVATIONS

Telescope	Line	Map Mode[a]	ΔV[b] (km s^{-1})	rms Noise[c] (K)	Grid Size (beams)	Field Size
Haystack	^{12}CO (1–0)	FB	0.81	0.66	7 × 7	1.7 × 1.7
	^{13}CO (1–0)	FB	0.15	1.0	7 × 7	1.8 × 1.8
	CS (2–1)	HB	0.027	4.8	7 × 7	1.0 × 1.0
FCRAO	^{12}CO (1–0)	FB	2.6	0.34	15 × 18	11.5 × 14
	^{12}CO (1–0)	HB	2.6	0.28	10 × 12	3.75 × 4.5
	^{13}CO (1–0)	FB	2.6	0.40	15 × 18	11.5 × 14
JCMT	^{12}CO (2–1)	FB	0.65	0.21	7 × 7	2.0 × 2.0
	^{13}CO (2–1)	FB	0.67	0.09	7 × 7	2.0 × 2.0

[a] FB = ful-beam sampled map; HB = half-beam sampled map.
[b] Velocity resolution.
[c] rms channel-to-channel noise in a single beam, corrected for telescope losses.

(110.20137 GHz) at the 14 m telescope of the Five College Radio Astronomy Observatory (FCRAO[6]) in 1991 June (Table 1). An additional map of ^{12}CO (1–0) was obtained in 1993 May to confirm and measure an anomalous pointing offset present in the 1991 data. The absolute position of the CO emission was established by referencing the emission to nearby SiO masers. The receiver system, QUARRY (Erickson et al. 1992), is a 5 × 3 array of Schottky mixers all tuned to a single rest frequency and placed at the Cassegrain focus. Detectors in the array are spaced by ∼50″ in R.A. and ∼100″ in decl. (HPBW is 45″ at 115 GHz). The back ends for each receiver were two 32-channel filter banks with filter widths of 1 MHz and 250 KHz, for velocity resolutions of 2.6 and 0.65 km s^{-1}, respectively. The filter banks were centered at the radial velocity of H_2O maser emission associated with IRS 1, V_{LSR} = +26 km s^{-1} (Paper I). Due to high humidity, typical system temperatures were ∼1500–2000 K. Integration times ranged from 2 minutes (^{13}CO) to 10 minutes (^{12}CO). After applying the pointing corrections established from the 1993 data, pointing accuracy is ∼10″. All antenna temperatures T_B presented here have been corrected for telescope and atmospheric losses.

We obtained 50″ or full-beam (FB) and 25″ or half-beam (HB) sampled maps of ^{12}CO (1–0) and a FB sampled map of ^{13}CO (1–0), with the position of IRS 1 serving as the reference position for each map. Data were obtained by position switching and subtracting a single 5 × 3 grid of off-source reference spectra from each on-source QUARRY grid in a given map; off-source positions (Galactic coordinates) were 17.6 + 1.2 for the ^{12}CO and ^{13}CO FB maps and 17.7 + 0.7 for the ^{12}CO HB map. Spectra were summed and baselines removed with the aid of the SPA software package at FCRAO.

2.2. *Haystack*

To construct higher spatial resolution ^{12}CO (1–0) and ^{13}CO (1–0) maps of a smaller region centered on IRS 1, we used the 37 m telescope of Haystack Observatory[7] (HPBW 20″ at 115 GHz). We also observed CS $J = 2 \rightarrow 1$ emission (97.9810 GHz). Data were obtained in 1993 February, following upgrades of the telescope surface and the receiver and correlator systems. These upgrades permit observations in the 3 mm wavelength range (Barvainis et al. 1993). Aperture efficiency at 115 GHz was estimated as ∼13% and beam efficiency as ∼18% at the elevation of peak gain. An SIS receiver was used in tandem with an autocorrelation spectrometer. Typical system temperatures were 250–300 K at 98 and 110 GHz and 400–600 K at 115 GHz. Integration times were 4 minutes for ^{12}CO and ^{13}CO and 2 minutes for CS. Based on contemporaneous position measurements of SiO masers, we estimate that blind pointing accuracy during these observations was ∼6″, with tracking accuracy of ∼2″.

Observing modes are listed in Table 1; we obtained 17″ or FB-sampled maps of ^{12}CO and ^{13}CO and a 10″ or HB-sampled map of CS. Spectrum bandwidths were 160 MHz for ^{12}CO, 53.3 MHz for ^{13}CO and 17.8 MHz for CS, with 512, 1024, and 2048 correlator lags, respectively. The central velocity was 22 km s^{-1}. Background emission was removed by frequency switching. This method of background subtraction proved to be more effective than position switching in producing flat baselines and, for the ^{12}CO observations, in avoiding confusion due to off-source Galactic emission. It also increased observing efficiency by eliminating off-source integration time. We used the LSR velocity range of ^{12}CO emission toward CRL 2136 as determined from the FCRAO spectra (∼10–50 km s^{-1}) to ensure that our switching throw at 115 GHz was sufficiently large (∼50 MHz) to avoid confusion between "positive" and "negative" signals. To account for the dependence of telescope gain on elevation, an elevation-dependent correction factor was applied to each spectrum. This correction factor is based on measurements of point sources and hence may overcompensate for gain loss at low elevations when applied to the extended emission from CRL 2136. Comparison with FCRAO data (§§ 3 and 4) indicates that the Haystack maps are well calibrated, however. After gain and beam efficiency correction, spectra at each position were averaged and baselines removed with the aid of the CLASS software package.

2.3. *JCMT*

Maps of the $J = 2 \rightarrow 1$ transitions of ^{12}CO (230.538 GHz) and ^{13}CO (220.399 GHz) were obtained at the 15 m James Clerk Maxwell Telescope (JCMT)[8] in 1991 June and 1992

[6] FCRAO is operated with support from National Science Foundarion Grant AST 91-15721 and the Commonwealth of Massachusetts with permission of the Metropolitan District Commission.
[7] Radio astronomy at Haystack Observatory is supported by a grant from the National Science Foundation.

[8] The James Clerk Maxwell Telescope is operated on a joint basis between the United Kingdom Science and Engineering Research Council (SERC), the Netherlands Organization for the Advancement of Pure Research (ZWO), the Canadian National Research Council (NRC), and the University of Hawaii (UH).

August. We obtained 7 × 7 20″ or FB-sampled maps of each isotopic species (Table 1). The observations in 1991 June were made in good weather conditions using the common user receiver RxA, a dual channel Schottky receiver with a receiver temperature of 500 K (DSB) resulting in system temperatures of ~900 K. During this period we obtained all ^{12}CO as well as nine ^{13}CO spectra with typical integration times of 6 min per position. The ^{13}CO observations were continued in 1992 August as a bad weather backup using RxA2, the new common user SIS receiver. These spectra had integration times of 2–5 minutes per position. RxA2 had a receiver temperature of around 150 K, but due to rather poor sky conditions the system temperature varied between 680 and 1500 K. Overlapping spectra show that the calibration between the two receivers is identical within errors. The backend was an acousto-optic spectrometer with a bandwidth of 500 MHz and a resolution of 0.5 MHz. Data presented here have been corrected for telescope losses assuming the forward scattering efficiency for both receivers is close to 0.8 and the main beam efficiency is ~0.65. The JCMT beam diameter at 230 GHz, 21″, is similar to that of Haystack at 115 GHz. Pointing was checked with five-point integrations on Uranus and nearby bright ultracompact H II regions and is accurate to a few arcsec. Background emission was removed by position switching; the (R.A., decl.) offsets of the off-source positions were (+15′, 0) for ^{12}CO and (+33.′3, −20′) for ^{13}CO. The ^{12}CO offset position was not clean. Therefore, we later measured the spectrum at this offset position and corrected all spectra for this emission. Also, as a check, we reobserved the center position using the clean offset position (+33.′3, −20′) and obtained very good agreement between the new spectrum and the previous, corrected spectrum.

Submillimeter and millimeter continuum observations were made at 450 and 800 μm and 1.1, 1.3, and 2.0 mm using the bolometer UKT14 (Duncan et al. 1990) at the JCMT in 1991 May and 1992 September. UKT14 is a sensitive ^{3}He-cooled one-channel bolometer with a filter wheel and a variable iris. Sky cancellation is achieved with a chopping secondary. The photometric observations reported here were made using the 65 mm (fully open) aperture and a 60″ east-west chop at a frequency of 7.8125 Hz. For a fully open aperture the HPBW of the telescope is roughly 18.″5, the largest deviation being for the 800 μm filter, where the HPBW is ~16.″8. Uranus was used as the primary flux calibrator, with assumed flux densities of 193.65, 83.75, and 50.64 Jy at 450, 800, and 1100 μm, respectively. In Table 2 we present a record of these observations. The uncertainty of about 8% in the zenith atmospheric optical depths is the dominant uncertainty in the measurements of most of the flux densities.

TABLE 2

SUBMILLIMETER/MILLIMETER CONTINUUM PHOTOMETRY

Filter	Observing Date	Zenith Optical Depth	Flux Density[a] (Jy beam^{-1})
2.0 mm	1992 Sep 25	0.040	0.48 ± 0.12
1.3 mm	1992 Sep 25	0.054	1.68 ± 0.05
1.1 mm	1992 Sep 25	0.069	2.35 ± 0.09
1.1 mm	1991 May 28	0.17	2.36 ± 0.04
800 μm	1992 Sep 25	0.345	6.66 ± 0.15
800 μm	1991 May 28	0.70	7.1 ± 0.2
450 μm	1991 May 28	2.6	72 ± 6

[a] Error-weighted results: 2.36 ± 0.04 at 1.1 mm and 6.82 ± 0.12 at 800 μm.

The 800 μm map, also obtained with UKT14, was made in 1991 July. Mapping was performed in horizontal coordinates in "on-the-fly" mode (Duncan et al. 1990) with a diffraction limited beam (HPBW ~ 13.″4), using a 30″ east-west chop, a sampling interval of 4″, and integration time of 1 s per pixel. Two maps, each with dimension just under 2′ in each coordinate direction, were made centered on CRL 2136 IRS 1. Uranus was mapped in the same way to determine the HPBW and error lobe contribution in a 60″ square area (~22% error lobe contribution). Each map was independently calibrated, restored, and transformed to equatorial coordinates using NOD2 (Haslam 1974).

2.4. *UKIRT*

A mosaic of 25 near-infrared images centered on CRL 2136 was obtained with the 3.8 m United Kingdom Infrared Telescope (UKIRT) in 1991 October. We used the infrared camera IRCAM, with a 62 × 58 InSb detector array, at a pixel scale of 1.″24. The filter was broad-band K (λ_c = 2.2 μm). Total exposure time was 60 s per image, the 60 s being made up of 12 co-added 5 s exposures. Dark current was removed from each image using a dark image of the same on-chip exposure time as the object images. Next, a flat field was created by median filtering the full set of 25 images. This flat field was then normalized to unity and divided into each of the object images. Bad pixels were removed by replacing them with the median of the eight adjacent pixels. Finally, the mosaic was pieced together based on the telescope offsets for each image.

3. RESULTS

3.1. ^{12}CO *and* ^{13}CO *Emission*

^{12}CO $J = 1 \rightarrow 0$ and $J = 2 \rightarrow 1$ spectra obtained toward various positions within 2′ of CRL 2136 display a strong, broad component centered at ~22 km s^{-1} and weaker components distributed from 32 to 50 km s^{-1} (Fig. 1). There is also a weak component at 13 km s^{-1} at some positions. The 22 km s^{-1} component is similar in radial velocity to strong OH mainline emission (Cohen, Baart, & Jonas 1988), CH and HCN emission (St. Clair Dinger et al. 1979), H_2O maser emission (Paper I), and methanol emission (V_{LSR} = 21 km s^{-1}; Menten & Reid, unpublished) detected toward the source. This component therefore probably is associated with CRL 2136 and/or its host molecular cloud, and suggests a kinematic distance of ~2 kpc (Paper I). Given the likelihood that the emission at 13 km s^{-1} and at 32 to 50 km s^{-1} is associated with closer and more distant molecular clouds along the line of sight, respectively (e.g., Fig. 3 in Dame et al. 1987), we restrict the scope of this paper to the 22 km s^{-1} component.

The intensity of ^{13}CO relative to ^{12}CO emission at the line core (Fig. 1) indicates that the core ^{12}CO emission is optically thick and that in some map positions the ^{12}CO is self-absorbed near line center. Self-absorption is more pronounced in Haystack ^{12}CO spectra than in FCRAO ^{12}CO spectra obtained at comparable spectral resolution (not shown), indicating that the absorption at a given velocity range arises in a region smaller than the FCRAO beam (i.e., $\lesssim$45″).

The 22 km s^{-1} ^{12}CO and ^{13}CO lines display wings that vary in intensity with position; this variation is more easily observed in the ^{13}CO (2–1) line profiles due to the complexity of individual ^{12}CO (2–1) spectra. North and west of IRS 1, the red wing is brighter and extends ~10 km s^{-1} from the line core, where it blends with the narrow background emission

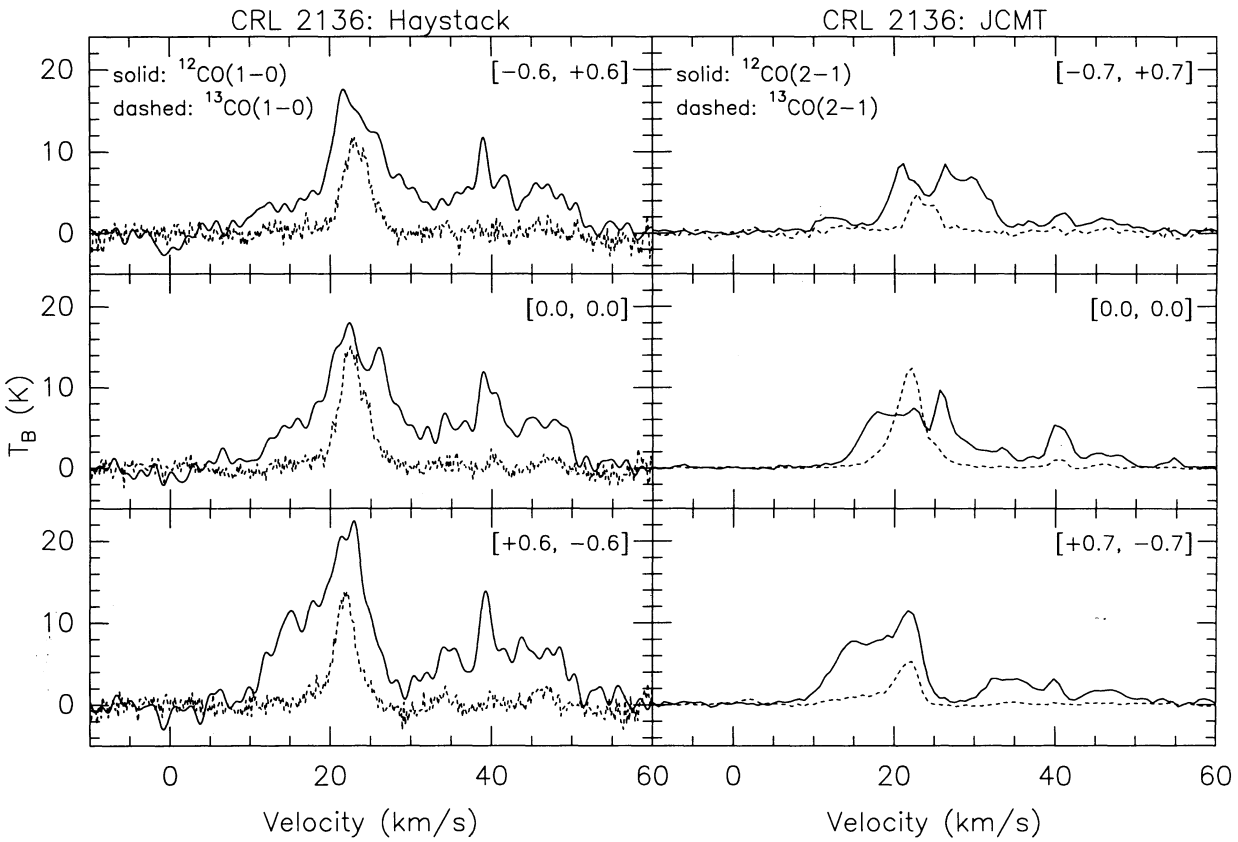

FIG. 1.—Spectra of ^{12}CO (*solid line*) and ^{13}CO (*dashed line*) emission obtained at Haystack (*left panels*; $J = 1 \rightarrow 0$ transition) and the JCMT (*right panels*; $J = 2 \rightarrow 1$ transition) toward selected positions near CRL 2136. Offset (arcmin) are indicated in the upper right corner of each panel. Emission centered at $\sim$22 km s^{-1} is from CRL 2136 and its associated cloud; emission between 32 and 50 km s^{-1} is probably due to background clouds. Moving from northwest to southeast of IRS 1 (*top to bottom panels*), the emission at 22 km s^{-1} changes from predominantly redshifted to predominantly blueshifted. This is most easily seen in ^{13}CO spectra since ^{12}CO is heavily self-absorbed. See § 3.1.

components. South and east of IRS 1 the blue wing becomes more pronounced and is $\gtrsim$10 km s^{-1} wide. The spatial variation of the line wings is seen clearly in position-velocity diagrams constructed from the ^{12}CO (1–0) maps. In Figures 2*a* and 2*b* we present such diagrams constructed from the FCRAO and Haystack data, respectively, for a cut along position angle −45°, perpendicular to the disk plane as inferred from near-infrared data (Paper I). In the lower resolution, wide-field FCRAO data, the line core emission is observed to peak near IRS 1, providing further evidence that the velocity component at 22 km s^{-1} is associated with the YSO. Line core emission, marginally resolved in the FCRAO data, appears in the Haystack diagram as a ridge centered near 22 km s^{-1}. In this diagram self-absorption on the blue side of the ^{12}CO line core to the southeast of IRS 1 shifts the peak intensity slightly redward of 22 km s^{-1}. Both diagrams show an abrupt change in the relative intensities of the line wings near the position of IRS 1, where the emission shifts from predominantly blueshifted to predominantly redshifted moving southeast to northwest. Figure 2*b* places this transition within $\sim$10″ of the YSO. The red wing emission, which extends $\sim$1′ NW of IRS 1, appears somewhat spatially truncated in comparison to the blue emission, which extends at least $\sim$2′ SE of IRS 1 (Fig. 2*a*).

We conclude from Figures 1 and 2 that (a) *the systemic velocity of the parent molecular cloud of CRL 2136 IRS 1 is* 22 ± 1 km s^{-1} and (b) *high-velocity redshifted emission* ($V_{LSR} \geq$ 24 km s^{-1}) *is located northwest of IRS 1, whereas high-velocity blueshifted emission* ($V_{LSR} \leq$ 20 km s^{-1}) *is largely confined to the southeast of IRS 1.* The latter conclusion suggests that an arcminute-scale bipolar molecular outflow emanates from the vicinity of IRS 1.

3.2. *Outflow Structure*

The morphology of the outflow is apparent in velocity-integrated maps constructed from the Haystack, JCMT, and FCRAO spectra (Figs. 3–6). The Haystack ^{12}CO and ^{13}CO maps (Fig. 3) illustrate the spatial separation of blueshifted and redshifted emission noted above. A bright condensation in blueshifted emission is also found to the WSW of IRS 1. This feature is best seen in the Haystack data integrated from 17 to 20 km s^{-1}, and lies approximately along a line connecting IRS 1 with the red lobe emission peak in the 24 to 27 km s^{-1} map. Similarly, weaker extensions to the ENE and SE are present in the red wing for this velocity range. Since the ^{12}CO emission is probably optically thick even in the line wings (§ 3.6), the ^{13}CO maps should give a more direct indication of the mass distribution in the cores of the outflow lobes. In these maps, blue lobe emission falls off most steeply to the northwest, whereas red lobe emission falls off most steeply toward the southeast. The Haystack map of ^{13}CO (1–0) emission integrated over the core velocity range (V_{LSR} = 20–24 km s^{-1}) shows that the emission peak lies $\sim$6″ SE of the position of IRS 1; the JCMT map of

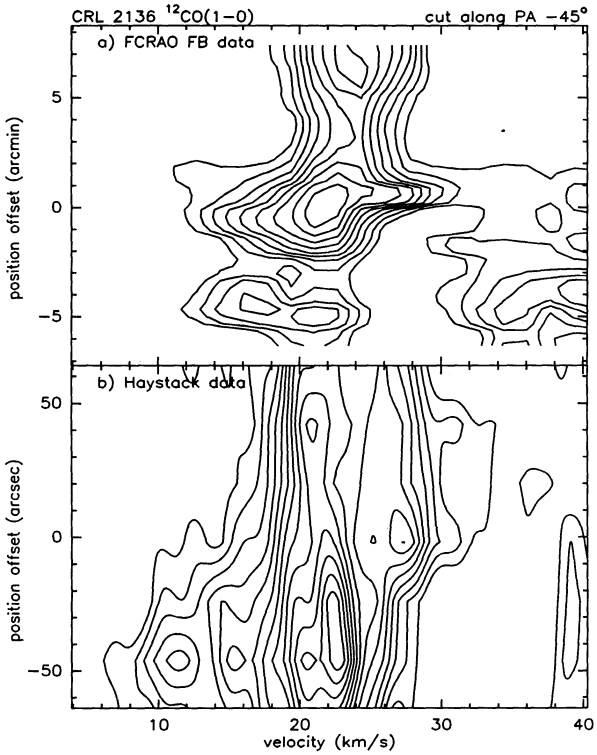

FIG. 2.—Position-velocity diagrams of ^{12}CO (1–0) emission for a cut through the position of IRS 1 running along position angle −45°. (*a*) FCRAO FB data. Lowest contour is 2 K and contours are at intervals of 1 K. (*b*) Haystack data. Lowest contour is 8 K and contours are at intervals of 1 K. Note the spatial separation of the line wings in both panels, indicating the presence of an arcminute-scale bipolar outflow centered on the YSO.

^{13}CO (2–1) displays a similar position offset for emission in the line core. It appears, therefore, that the peak ^{13}CO emission and the position of IRS 1 are not coincident. The displacement of the ^{13}CO peak to the SE of IRS 1 is consistent with the relative position of the centroid of peak CS emission (§ 3.4). The peak contours of ^{13}CO line core emission appear slightly elongated northeast-southwest. The ^{13}CO line core map also shows a ridge of emission extending due west at declination offset $\sim -25''$. This ridge is roughly spatially coincident with the ridge of blue-wing ^{12}CO emission.

Overall, the JCMT CO (2–1) maps (Fig. 3) reveal features very similar to those observed in the Haystack (1–0) maps. The western blue peak and the bridge connecting it to the southeast blue peak are especially prominent in the ^{12}CO (2–1) maps. Like ^{13}CO (1–0), the centroid of ^{13}CO (2–1) emission shifts from the southeast for $V_{LSR} \leq 20$ km s^{-1} to the northwest for $V_{LSR} \geq 24$ km s^{-1}, with the steepest gradients in each lobe directed toward the opposite lobe. The morphology of red lobe ^{13}CO (2–1) emission is very similar to that at (1–0). The blue-shifted ^{13}CO (2–1) displays a sharp peak at offsets (0″, −25″), near the peak of the ^{13}CO (1–0) map for the same velocity range, suggesting the optical depth of the blue lobe is large toward this offset. The line core ^{13}CO (2–1), like (1–0), displays a ridge extending west at $\sim -25''$.

In Figures 4–6, we present ^{12}CO (1–0) maps integrated over the range of high-velocity emission. Each feature in the Haystack map (Fig. 4) is reproduced at lower resolution in the HB FCRAO map (Fig. 5), and the gross features (in particular, the position angle of a line joining the red and blue lobe emission peaks) are in turn reproduced in the FB FCRAO map (Fig. 6), confirming the orientation of the blue and red outflow lobes within $\sim 2'$ of IRS 1. Like the Haystack and JCMT maps, the HB FCRAO map also shows a prominant blue-wing extension and secondary peak to the WSW of IRS 1. In Figures 4 and 5 we see that, within the pointing accuracy of the respective telescopes, a line connecting the red and blue emission peaks passes through the YSO. These maps, and the maps constructed from JCMT spectra, therefore strongly implicate IRS 1 as the driving source of the outflow. From Figures 4–6, we estimate a peak-to-peak position angle (blue to red lobe) of 120°–150° and a peak-to-peak lobe separation of $\sim 1'.2$ for the ^{12}CO emission. Hence the outflow axis appears to lie nearly perpendicular to the "polarization disk" plane (Paper I) and is sufficiently inclined with respect to the plane of the sky so as to produce spatially separated redshifted and blueshifted emitting regions.

Figure 7 (Plate 22) shows the FCRAO HB map of high-velocity ^{12}CO emission superposed on the *K*-band mosaic obtained with UKIRT. The reflection nebulosity within $\sim 45''$ of IRS 1 was discussed in detail in Paper I and Minchin et al. (1991). In addition to the Juggler nebula at the center of the mosaic, hundreds of stellar (point) sources and two additional regions of nebulosity (one lying partly off the top of the frame and one at offsets $[-0'.9, -1'.5]$) appear in the mosaic. The comparison with CO emission appears to show that, generally, the regions of lowest stellar surface density are correlated with the strongest CO. The surface density of stars is particularly low to the NNW of CRL 2136. This suggests that the stars in the field are primarily background sources whose apparent surface density is modulated by foreground extinction in the CRL 2136 cloud. Hence the large-field image may contradict the suggestion (Paper I) that the stellar sources within $\sim 45''$ of IRS 1 are members of a young cluster associated with the YSO. Figure 7 suggests instead that there are no other YSOs brighter than $K \sim 14$ (the approximate limiting magnitude of the image) within $\sim 1'$ of IRS 1. Although this result requires confirmation through multicolor near-infrared imaging of a larger region surrounding IRS 1, the apparent isolation of the YSO would make it rare among regions of massive star formation (Carpenter et al. 1993). The figure also illustrates that the apparent outflow axis is closely aligned with the west and south scattering lobes of the Juggler nebula (as defined in Paper I), whereas the east scattering lobe and associated near-infrared "jet" extending due east from IRS 1 appears to have no direct analog in the CO map.

3.3. *Large-Scale* CO *Emission*

Beyond the inner regions where data from all three radio telescopes overlap, the FB FCRAO map shows the outflow lobes blending into extensive regions of redshifted and blue-shifted ^{12}CO (1–0) emission, respectively, north and south of CRL 2136 (Fig. 6). These regions extend approximately N–S out to displacements $\sim 5'$ from IRS 1, beyond which they expand in the E-W direction and contain secondary emission peaks. If this "lobe" emission were all part of the bipolar outflow from CRL 2136, this protostellar outflow would easily be the largest such structure known in the Galaxy, with an end-to-end projected length $\gtrsim 6$ pc. The shift in the central velocity of ^{12}CO (1–0) emission at offsets $\gtrsim 2'$ from IRS 1 (Fig. 2*a*), however, indicates that some or all of the "lobe" emission at very large displacements ($\gtrsim 3'$) from IRS 1 can be attributed

PLATE 22

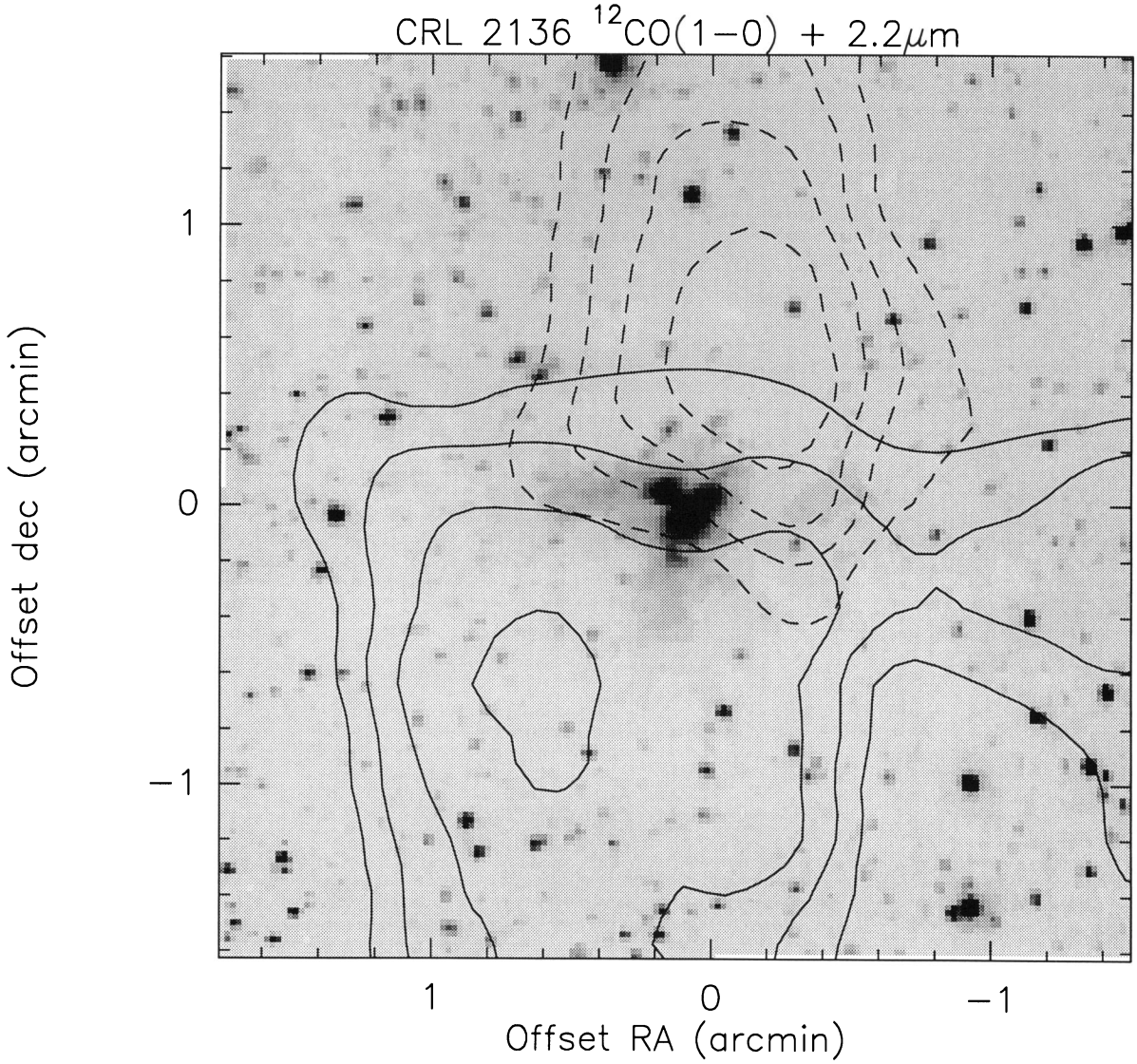

FIG. 7.—FCRAO CO map of Fig. 5, overlaid on a mosaic of 2.2 μm images of the CRL 2136 region obtained at UKIRT. The outflow morphology appears to follow that of the south and west lobes of the reflection nebula. Two other extended, nebulous regions appear in the image, one ~1'.5 N and one ~1'.5 SSW of IRS 1. The density of infrared point sources appears to be lowest near the nebula, especially to the northwest of IRS 1; generally, the point source density and CO intensity appear to be anticorrelated, suggesting most or perhaps all of the point sources are background stars.

KASTNER et al. (see 425, 699)

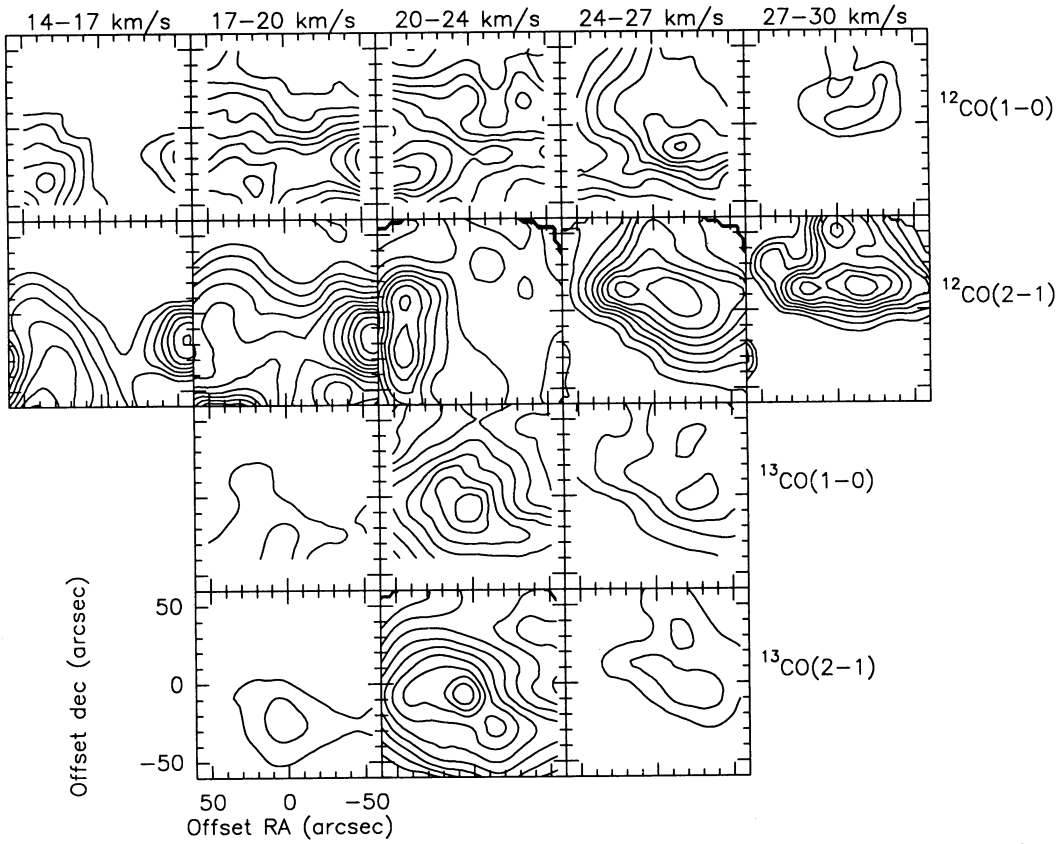

FIG. 3.—Maps of CO emission constructed from velocity-integrated Haystack and JCMT spectra. The velocity interval is indicated at the top of each column of panels. For Haystack maps (first and third rows), contours of ^{12}CO (1–0) are from 18 K km s^{-1} to a peak of 84 K km s^{-1} at offsets (+45″, −30″) in the center panel, and contours of ^{13}CO (1–0) are from 6 K km s^{-1} to a peak of 54 K km s^{-1} at offsets (+3″, −8″) in the center panel. For JCMT maps (second and fourth rows), contours of ^{12}CO (2–1) are from 9 K km s^{-1} to a peak of 44 K km s^{-1} at offsets (+45″, −25″) in the center panel, and contours of ^{13}CO (1–0) are from 6 K km s^{-1} to a peak of 38 K km s^{-1} at offsets (+5″, −7″) in the center panel. Contour intervals are 3 K km s^{-1} in all maps. The beam diameters of the two telescopes are similar (20″) at the respective transitions of CO. In all four map sequences, the emission centroid moves from SE to NW with increasing velocity (§ 3.2).

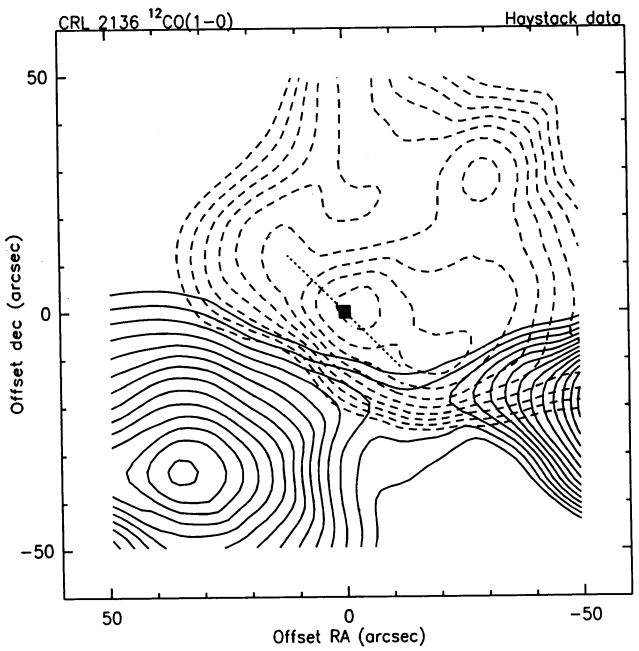

FIG. 4.—Map constructed from Haystack ^{12}CO data showing velocity-integrated emission from the blue lobe (*solid contours*; velocity range 14 to 20 km s^{-1}) and red lobe (*dashed contours*; velocity range 24 to 30 km s^{-1}). The lowest contour is at 52 K km s^{-1} and the contour interval is 2 K km s^{-1}. The position of IRS 1 is indicated by the solid square at offsets (0, 0) and the approximate position angle of the "polarization disk" is indicated by the short-dashed line (§ 3.2).

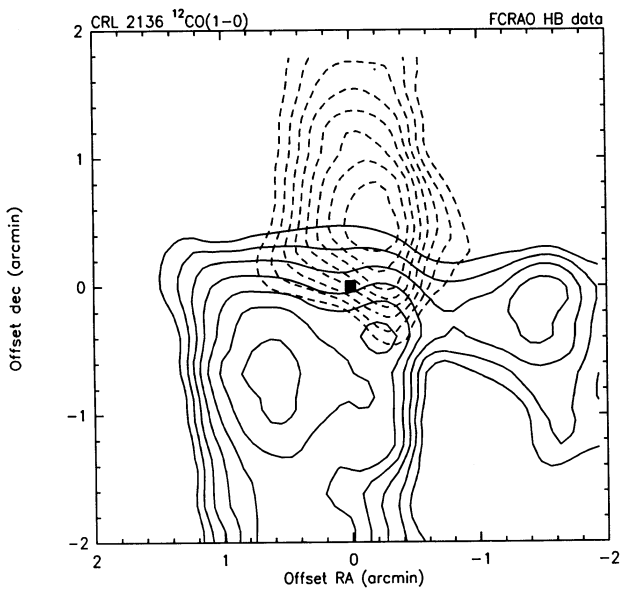

FIG. 5.—Same as in Fig. 4, for HB-sampled FCRAO ^{12}CO data. The lowest contour is at 18 K km s^{-1} and the contour interval is 2 K km s^{-1}. Each feature in the Haystack map is reproduced at lower resolution in this figure, confirming the detailed morphology of the inner blue and red lobes.

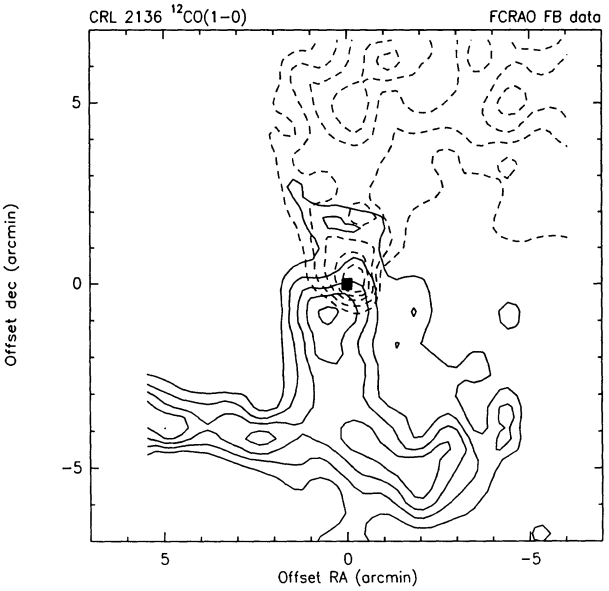

FIG. 6.—Same as in Fig. 4, for FB-sampled FCRAO ^{12}CO data. The lowest contour is at 14 K km s^{-1} and the contour interval is 4 K km s^{-1}. Redshifted and blueshifted emission beyond ~2′ from IRS 1 probably reflects large-scale cloud motions (§ 3.3).

to a large-scale velocity gradient in the ambient cloud material. This emission therefore is probably not directly associated with the outflow. The presence of a large-scale gradient is seen more clearly in psotion-velocity diagrams constructed from the FCRAO ^{13}CO (1–0) maps (Fig. 8). The central velocity of ^{13}CO emission varies with declination from ~20 km s^{-1} 5′ S of IRS 1 to ~24 km s^{-1} 3′ N of IRS 1. A velocity gradient of similar magnitude is seen with R.A. These gradients probably reflect bulk motions of the cloud such as rotation or shear (§ 4.3). Even ignoring emission beyond 1′ NW and 2′ SE of IRS 1, however, the end-to-end projected length of the CRL 2136 outflow is ~2 pc, making it one of the largest such structures known (§ 4.2).

3.4. CS *Emission*

CS (2–1) emission is distributed throughout most of the region covered by the Haystack map (Fig. 9 [Pl. 23]). Studies by Snell et al. (1984a) and Mundy et al. (1986) have established that such emission generally traces the densest regions of a molecular cloud core. Thus it appears that IRS 1 and the Juggler nebula lie very near the position of such a core, as was inferred from multicolor near-infrared imaging (Paper I). Like the line-core ^{13}CO (1–0) and (2–1) emission, however, the centroid of peak CS emission appears to be displaced SE of the position of IRS 1.

No line wings are evident in the CS spectra. The core emission, however, shows a slight velocity gradient, with a velocity of 22.1 ± 0.1 km s^{-1} (mean and error on the mean) in a 20″ × 20″ region SE of and adjacent to IRS 1, and a velocity of 23.4 ± 0.1 km s^{-1} in the same size region NW of and adjacent to the YSO. The analogous regions NE and SW of IRS 1 display mean velocities of 22.4 and 22.6 km s^{-1}, respectively, which are intermediate between the SE and NW regions and are the same to within the uncertainties. Thus it appears that the emitting CS gas displays the same kinematic signature observed at large scales in CO (§§ 3.3 and 4.3).

3.5. *Submillimeter Thermal Emission*

The 800 μm thermal continuum map of the inner ~2′ × 2′ region is presented in Figure 10. The continuum source is elon-

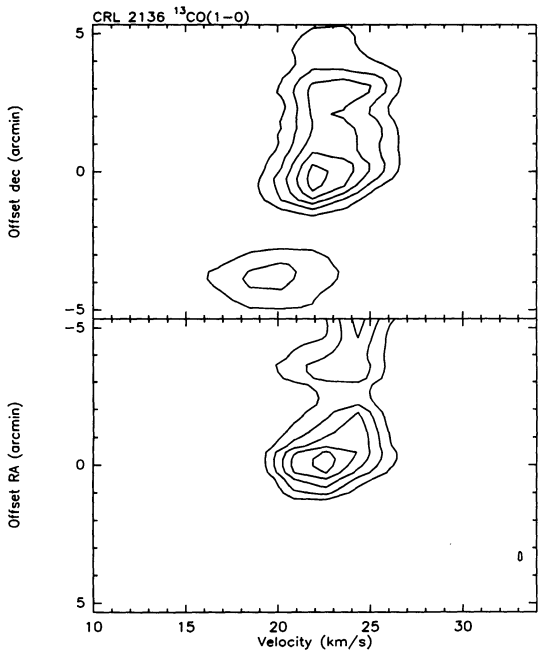

FIG. 8.—Position-velocity diagrams for cuts through the FB FCRAO ^{13}CO map in decl. (at the R.A. of IRS 1) (*top*) and R.A. (at the decl. of IRS 1) (*bottom*). A velocity gradient is evident in both diagrams, with emission toward the north and west redshifted with respect to the systemic velocity of CRL 2136 (22 ± 1 km s^{-1}).

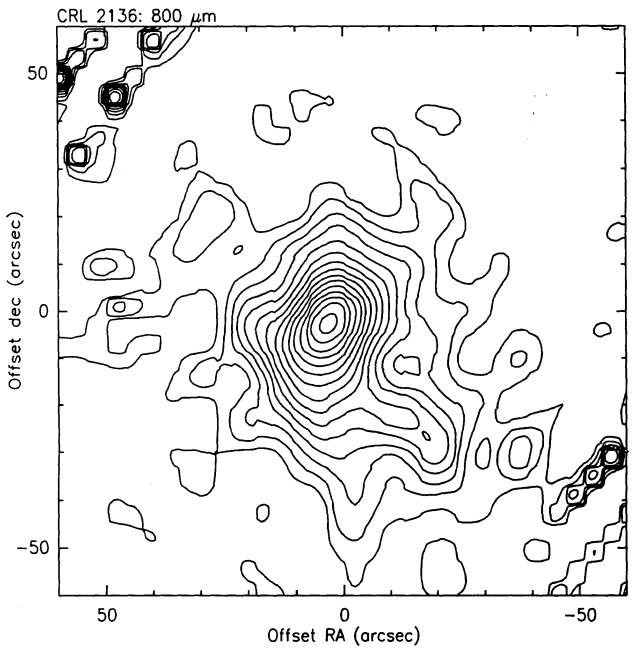

FIG. 10.—JCMT map of 800 μm continuum emission from CRL 2136. Contours are from 0.4 Jy beam^{-1} at intervals of 0.4 Jy beam^{-1} (HPBW 13″.4). The emitting region appears to be slightly elongated SE–NW, and a ridge of emission meanders westward 25″ S of the main peak (this ridge also appears in maps of line core ^{13}CO emission; Fig. 3). The emission peak is offset a few arcsec SE of IRS 1.

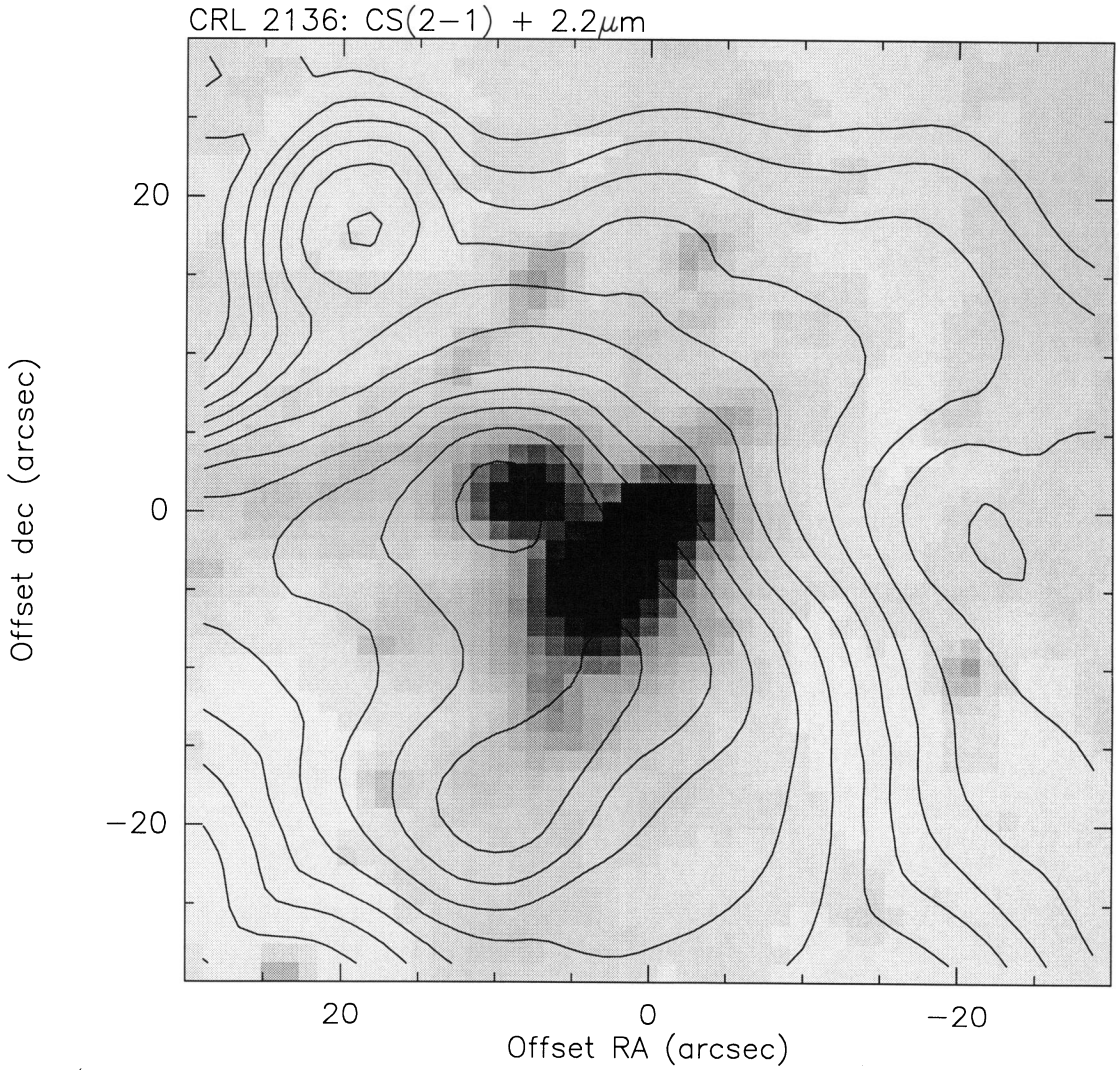

FIG. 9.—Map of CS (2–1) emission constructed from Haystack spectra integrated from 20 to 24 km s^{-1}, overlaid on a 2.2 μm image obtained with an infrared camera at the Kitt Peak 2.1 m telescope (Paper I). Contours are from 8 K km s^{-1} at intervals of 2 K km s^{-1}. The emission centroid is displaced $\sim 10''$ SE of IRS 1.

KASTNER et al. (see 425, 701)

gated along the northwest-southeast direction, approximately parallel to the outflow axis established by the CO data. A Gaussian fit to the extended emission source gives a size of $26'' \times 17''.9$ at position angle $-14°.3$ and a positional offset of the peak from IRS 1 of $+3''$ in R.A. and $-2''$ in decl. This offset is smaller than, but in the same direction as, positional offsets between IRS 1 and the positions of peak ^{13}CO (§ 3.2) and CS (§ 3.4) emission. The apparent size corresponds to a deconvolved size of $22''.2 \times 11''.8$, or a geometric mean of $16''.2$, i.e., a radius of $8''$. A prominent extension stretches at least $30''$ to the southwest of the 800 μm emission core; this extension appears to be spatially coincident with the ridge seen at line center in ^{13}CO (Fig. 3). The long wavelength thermal emission apparently maps the concentration of heated dust near IRS 1. This dust is locally resident in the molecular cloud and/or is entrained by the gas in the molecular outflow (§ 4.2).

For the resolved source we obtain 15.5 Jy from the map. This compares well to the photometry predicted (13.8 Jy) by extrapolating the 800 μm photometric result (6.82 Jy beam^{-1}) according to resolved source size. The integrated flux (corrected for error lobe pickup) is 23.3 Jy in a $60'' \times 60''$ region and 28.7 Jy in a $120'' \times 120''$ region.

3.6. CO *Optical Depths and Excitation*

Measurements of ^{12}CO and ^{13}CO in both the $J = 1 \rightarrow 0$ and $J = 2 \rightarrow 1$ transitions allow a determination of the excitation temperature of ^{12}CO (T_{ex}) that, in principle, is independent of the assumed ^{13}CO/^{12}CO abundance ratio X (Snell et al. 1984b; Plambeck, Snell, & Loren 1983). We applied the method described by Snell et al. to estimate T_{ex} for the high-velocity gas in overlapping regions of the Haystack and JCMT maps. This method involves using the ratios of ^{12}CO to ^{13}CO line intensities (referred to as R_{10} and R_{21} for the $J = 1 \rightarrow 0$ and $J = 2 \rightarrow 1$ transitions, respectively) to derive optical depths. Since the method relies on intensity ratios, it is relatively insensitive to the absolute calibration of the data if both isotopic species are measured with the same telescope, even if the two transitions are measured with different telescopes.

If the ^{12}CO emission is optically thick, the ^{13}CO emission is optically thin, and the excitation temperatures of ^{12}CO and ^{13}CO are equal, then the ratio of optical depths in the $J = 1 \rightarrow 0$ and $J = 2 \rightarrow 1$ transitions can be related to the intensity ratios by

$$\frac{R_{10}}{R_{21}} = \frac{\tau_{21}}{\tau_{10}} . \quad (1)$$

From the ratio of optical depths one can derive T_{ex} from

$$\frac{\tau_{21}}{\tau_{10}} = \frac{2[1 - \exp(-h\nu_{21}/kT_{ex})]}{\exp(h\nu_{10}/kT_{ex}) - 1} . \quad (2)$$

For the high-velocity gas (integrated from 10 to 20 km s^{-1} for the blueshifted gas and from 24 to 34 km s^{-1} for the redshifted gas), the velocity integrated ^{12}CO/^{13}CO intensity ratios R_{10} and R_{21} typically have values between 5 and 10. Thus, if the isotopic ratio is roughly terrestrial ($X = 89$) and the excitation temperatures of ^{12}CO and ^{13}CO are the same, then ^{12}CO is optically thick and the ^{13}CO optical depths are small, typically 0.1 to 0.2. The isotopic ratio would have to be substantially smaller than terrestrial to change these results. The ratio R_{10}/R_{21} in the high-velocity gas has values ranging from about 0.8 to 1.8. From these ratios we find that T_{ex} is approximately between 5 and 10 K, with the result for the blue lobe very uncertain due to low signal-to-noise in the Haystack ^{13}CO spectra.

If the gas is thermalized, then T_{ex} should equal the gas kinetic temperature and our results would imply gas temperatures only 5 to 10 K, slightly lower than those found for other molecular outflows from massive YSOs (e.g., Snell et al. 1984b). However, the main beam brightness temperature of the ^{12}CO emission within the velocity range integrated for the high-velocity gas is greater than 10 K at some locations (Fig. 1). Thus it is unlikely that the excitation temperature of the gas is as low as implied by the optical depth ratios. The ratios R_{10} and R_{21} could be affected by differences between ^{12}CO and ^{13}CO in either their excitation temperatures or beam filling factors. Given either effect, the ^{13}CO line may have much higher optical depths than we estimated. In fact there is good evidence that molecular outflows may be clumpy (Plambeck et al. 1983; Snell et al. 1984b) and thus may produce different filling factors in the two isotopic species. If the isotopic ratios mainly reflect differences in excitation or beam filling, then the excitation temperature of the gas can be seriously underestimated.

3.7. *Molecular and Dust Masses*

In Table 3 we list H_2 masses for the outflow lobes and for the line core emission as estimated from the velocity-integrated intensities of ^{12}CO (1–0) emission and the ratio of ^{13}CO to ^{12}CO (1–0) line intensities. The latter quantity allows us to correct the mass estimates for the ^{12}CO optical depth (Cabrit, Goldsmith, & Snell 1988). We calculated masses from the FCRAO spectra integrated over the velocity range 14 to 30 km s^{-1}. Hence the cloud mass estimates (Table 3B) include both high-velocity and line core emission, although the mass in high-velocity gas constitutes less than 10% of the cloud mass within regions larger than ~ 20 arcmin^2 centered on IRS 1. For

TABLE 3A

TEMPERATURES AND MASSES DERIVED FROM CO DATA: OUTFLOW LOBES[a]

Lobe	V Range (km s^{-1})	R.A. Range[b]	Decl. Range[b]	Mass ($M_\odot$)
Blue	+10, +20	+1:0, 0:0	−1:0, 0:0	21
		+0.3, 0.0	−0.3, 0.0	6
Red	+24, +34	0.0, −1.0	0.0, +1.0	29

TABLE 3B

TEMPERATURES AND MASSES DERIVED FROM CO DATA: CLOUD[c]

Size of Region	R[d] (pc)	Mass ($M_\odot$)	V_K[e] (km s^{-1})
1:7 × 1:7	0.5	270[a]	...
2 × 2	0.6	240	1.3
4 × 4	1.2	480	1.3
8 × 8	2.4	1200	1.5
12 × 12	3.6	2500	1.7

[a] Estimated from Haystack data.
[b] Offsets relative to the position of IRS 1.
[c] Masses within regions centered on IRS 1, estimated from FCRAO data unless otherwise noted. Estimates are for combined mass in line core and high-velocity emission.
[d] Approximate equivalent radius of region.
[e] Predicted velocity for Keplerian motion.

the line core, we assumed an excitation temperature of 10 K for the CO gas, whereas we adopted $T_{ex} = 5$ K for the high-velocity emission (§ 3.6). The results are not very sensitive to the assumed values of T_{ex}, however, with $M \propto T_{ex}^{1/3}$ in the regime 5 K $< T_{ex} <$ 15 K. For the mass estimates, we assume $X = 89$ and $[^{12}CO]/[H_2] = 2 \times 10^{-4}$.

The results indicate that $\sim 50\ M_\odot$ of molecular gas resides in the regions of high-velocity gas mapped at Haystack, compared to a line-core mass of $\sim 220\ M_\odot$ in these regions. The total mass estimated for a similar-sized region within the FCRAO maps agrees very well given the uncertainties in the respective telescope calibrations. The FCRAO data further indicate that the molecular cloud containing CRL 2136 possesses $\sim 2500\ M_\odot$ within a region ~ 3.6 pc in radius centered on IRS 1. Thus we find that the 4 arcmin^2 region surrounding the YSO, a region comprising less than 3% of the projected surface area mapped with QUARRY, harbors more than 10% of the mass within this surface area. It is possible that this mass concentration exerts considerable influence over the large-scale kinematics of the cloud (§ 4.3).

In Figure 11, we present a plot of the spectral energy distribution (SED) of the Juggler nebula from 1 μm to 2 mm. The plot includes large beam measurements made from rocket and space platforms and groundbased instruments. Overlaid on the SED are results for an isothermal model of the Juggler nebula. In this model we assume the dust grains can be characterized by a single dust temperature, T_d. The flux density at frequency ν measured at the telescope is then given by (Sandell & Weintraub 1994)

$$F_\nu = \Omega_s B_\nu(T_d)(1 - e^{-\tau_\nu}) , \quad (3)$$

where Ω_s is the source solid angle, B_ν is the Planck function, and τ_ν is the optical depth at ν. We write τ_ν as

$$\tau_\nu = \tau_0\left(\frac{\nu}{\nu_0}\right)^\beta , \quad (4)$$

where τ_0 is the dust optical depth at frequency ν_0 and β is the dust emissivity index. To estimate the total dust mass, M_d, we use the Hildebrand (1983) formulation for the grain opacity

$$\kappa_\nu = \kappa_0\left(\frac{\nu}{\nu_0}\right)^\beta \quad (5)$$

where κ_0 is the value of the grain opacity at the specified frequency ν_0, and a numerical expression derived by Sandell & Weintraub (1994),

$$M_d = 1.88 \times 10^{-4}\left(\frac{1200}{\nu}\right)^{3+\beta} F_\nu(e^{0.048\nu/T_d} - 1)D^2 , \quad (6)$$

where ν is given in GHz, F_ν in Jy, T_d in K, D in kpc, $\kappa_0 = 10$ cm^2 g^{-1} at $\nu_0 = 1200$ GHz (250 μm), and M_d is given in solar masses.

At submillimeter wavelengths, emission from hot dust emitting at mid-infrared wavelengths largely can be neglected because of the small angular size of the hot dust region. Thus, we use only data from $\lambda > 50$ μm in our model fit. The 800 μm map shows that the source is extended relative to the submillimeter and millimeter HPBWs. Therefore we use the observed source size to further constrain the fit by assuming the source shape is Gaussian with FWHM equal to the geometric mean of the measured FWHM in R.A. and decl. After correcting for source size, we make a least-squares fit to equa-

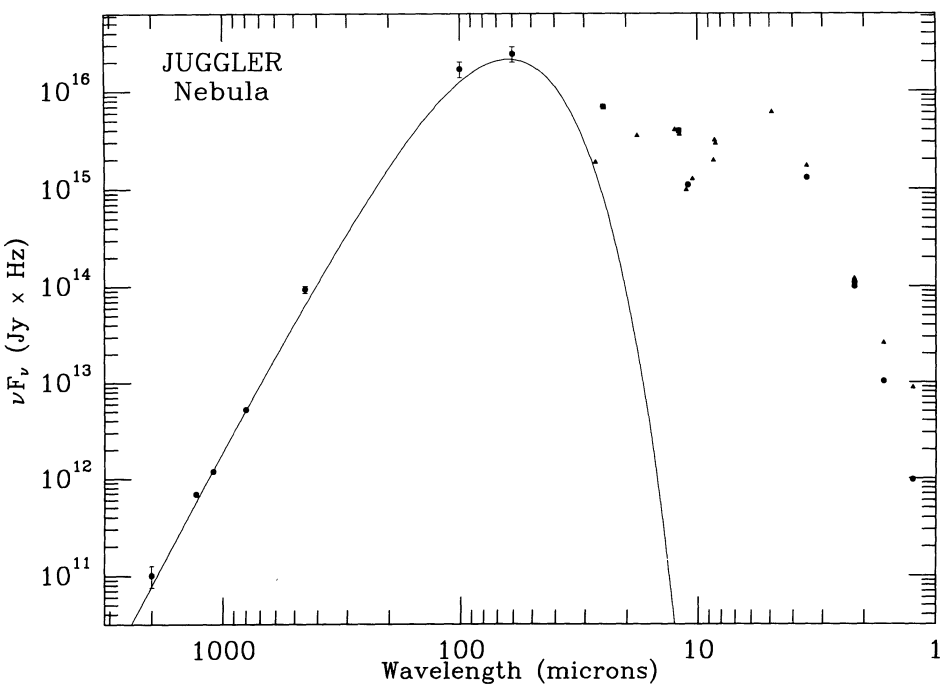

FIG. 11.—Spectral energy distribution of CRL 2136 from 1.25 μm to 1100 μm. Shown are photometry from Allen et al. (1977; *circles at* 1.25, 1.65, 2.2, *and* 3.5 μm); Paper I (*circle nearly coincident with Allen et al. data for* 2.2 μm); *IRAS* survey (*circles at* 12, 25, 60, and 100 μm); Lebofsky et al. (1976; *circle at* 11 μm); AFGL survey (Ney & Merrill 1980; Price & Murdock 1983; *triangles*); and this paper (*points longward of* 100 μm). Error bars are indicated for *IRAS* and submillimeter data. Discrepancies between mid- and near-infrared photometry at a given wavelength may be due to differences in aperture sizes and/or placements (Paper I). Overlaid on the data is the flux distribution of an isothermal model with $M_d = 1.35\ M_\odot$, $T_d = 40.6$ K, radius 8″, and $\beta = 1.72$ (§ 3.7).

tion (3) which includes three free parameters: β, Ω_s, and T_d. We obtain our first model result without any far-infrared data, since such observations have poorer spatial resolution and, if the source is extended at far-infrared wavelengths, will overestimate the flux densities. In this case, after constraining the source diameter to be 16".2 at $T_d = 60$ K, we find $\beta = 1.65$ and $M_d = 0.78\ M_\odot$. If we include *IRAS* 60 and 100 μm data and leave T_d unconstrained, we obtain a best fit $\beta = 1.72$, $T_d = 40.6$ K and $M_d = 1.35\ M_\odot$. Since the value of κ_0 assumed here may be somewhat large (Draine & Lee 1984), $M_d \sim 1\ M_\odot$ probably represents a rough lower limit for the thermal dust mass within $\sim 8''$ (or 16,000 AU) of IRS 1. This result is about an order of magnitude larger than the scattering dust mass estimated for a slightly larger region surrounding the YSO (Paper I). The integrated luminosity from 150 to 30,000 GHz is $7.2 \times 10^4\ L_\odot$, which compares well with that estimated in Paper I ($5 \times 10^4\ L_\odot$).

4. DISCUSSION

4.1. *Orientation of the Outflow*

The maps of high-velocity CO emission (Figs. 3–6) reveal a poorly collimated outflow that nonetheless appears to be aligned with the polar axis of the IRS 1 system as inferred from near-infrared maps of linear polarization (Paper I). The molecular line data therefore strongly support the interpretation that the elliptical patterns of near-infrared polarization within $\sim 5''$ of IRS 1 are due to multiple scattering within an optically thick disk. In Paper I, we further argued that the dependence of polarization on wavelength in the near-infrared provided evidence that the disk plane of the CRL 2136 system was oriented nearly perpendicular to the plane of the sky, which in turn would indicate that the polar axis lies roughly parallel to the plane of the sky. The maps of high-velocity emission suggest, however, that the polar axis has at least a modest inclination, such that the southeast outflow lobe is closer to the Earth than the northwest lobe. The CO data are therefore consistent with the model described by Minchin et al. (1991), who suggested that the bright southeasterly extensions of the near-infrared nebula are closer to the observer than the fainter northwestern extensions. The comparison between the morphologies of the high-velocity emission and the near-infrared reflection nebulsity (Fig. 7) reinforces this conclusion. The apparent wide opening angle of the outflow also appears consistent with the interpretation of the E and SE near-infrared lobes as the limbs of a single, forward-scattering, bubble-like lobe (Minchin et al.). We are unable to rule out the hypothesis of multiple outflow axes (Paper I) or a bifurcated flow (see below), however.

While the molecular line data suggest that the polar axis is inclined with respect to the plane of the sky, they also suggest that the inclination is not large. The overlap of contours of redshifted and blueshifted emission in the vicinity of IRS 1 (Fig. 4), the prominent blue-lobe extension to the WSW (Figs. 4 and 5), and the weaker red-lobe extension to the ENE (Fig. 3) suggest that there are components of the predominantly redshifted lobe that point toward the observer, and components of the predominantly blueshifted lobe that point away (assuming the system does not contain multiple outflows). This would be the case for an inclination angle that is smaller than the opening angle of the lobes (Cabrit & Bertout 1990). Indeed, the large-scale velocity and spatial structure of the outflow as revealed in the FCRAO data (Figs. 2*a* and 5) bears a resemblance to the Cabrit and Bertout model of an outflow that has an opening angle of 60° and an inclination of 40° with respect to the plane of the sky (their Case 4). This suggests that the inclination of the outflow is $\sim 40°$ or possibly smaller if the outflow follows parabolic rather than conic streamlines (Meyers-Rice & Lada 1991). The correspondence between the Cabrit and Bertout model and our data is not perfect; in particular, the CRL 2136 outflow does not exhibit well-defined contamination of the red and blue lobes by blueshifted and redshifted emission, respectively, far out in the outflow. We note, however, that the apparent southeasterly offsets of the line core ^{13}CO, CS and submillimeter emission peaks from the position of IRS 1 suggest that cloud inhomogeneities may play a role in shaping the outflow. In particular, the forward-facing southeast outflow lobe may widen or split as it encounters dense ambient material concentrated $\sim 10{,}000$ AU from IRS 1.

If the 3.1 μm water ice absorption feature (Willner et al. 1982) arises in a circumstellar disk surrounding IRS 1, as proposed in Paper I, then our detection of spatially separated blueshifted and redshifted lobe emission places constraints on the geometry of the disk. Specifically, if the inclination of the polar axis with respect to the plane of the sky is $\sim 40°$, this would suggest that the disk is very thick or highly flared.

4.2. *Outflow Scale, Mass, Gas-to-Dust Ratio and Age*

The results of § 3 suggest the molecular outflow from CRL 2136 IRS 1 is one of the largest and most massive YSO outflows known. The total projected length of the outflow, ~ 2 pc, is on the order of that of outflows from NGC 7538 IRS 1, W49 (Scoville et al. 1986) and DR 21 (Russell et al. 1992; Garden et al. 1991). Its estimated mass, $\sim 50\ M_\odot$, is similar to or greater than that of most outflows associated with well-studied massive star-formation regions (e.g., NGC 2071, CRL 490, Orion IRc2, and NGC 7538 IRS 1; Snell et al. 1984a, b; Scoville et al. 1986), with W49 and DR 21 being notable exceptions.

The molecular mass within a region comparable in area to the S and E scattering lobes of the infrared Juggler nebula is $\sim 6\ M_\odot$ (Table 3A). If the total mass of scattering grains in these regions ($\sim 0.07\ M_\odot$; Paper I) represents most of the dust mass entrained in the outflowing gas, this would suggest that the thermal dust mass estimated from submillimeter continuum emission ($\sim 1\ M_\odot$ within $\sim 8''$ of IRS 1; § 3.7) is dominated by contributions from grains in the ambient cloud and/or the presumed circumstellar disk. In this case, the implied gas-to-dust mass ratio in both outflow and cloud material near IRS 1 would be ~ 100, i.e., similar to the typical interstellar value. If the estimate from submillimeter continuum emission better represents the entrained dust mass, however, this would suggest the grains seen in scattered light at 2 μm represent only a small fraction of the total dust mass in the outflow, and that the outflow from CL 2136 IRS 1 is much dustier than typical of interstellar clouds. We are unable to use our data to distinguish definitively between these hypotheses, although the 800 μm morphology (Fig. 10) appears more consistent with the interpretation that the submillimeter emission arises in the outflow.

Despite the enormous size and mass of the CRL 2136 outflow, the likely driving source IRS 1 probably is surrounded by one of the least luminous H II regions known among massive outflow sources (Henning, Pfau, & Altenhoff 1990; Kurtz et al. 1994). Thus IRS 1 is probably one of the youngest high-mass YSOs known to possess an outflow. With a dynami-

cal age $\sim 10^5$ yr (adopting a projected outflow velocity of 10 km s^{-1} and assuming an inclination of 40°), the outflow appears much older than IRS 1 (age $\lesssim 10^4$ yr, as estimated from "classical" theoretical evolutionary tracks; Paper I) unless the molecular gas has decelerated substantially. These observations, like those of the low-mass protostar VLA 1623 (André, Ward-Thompson, & Barsony 1993), therefore offer evidence that bipolar outflows might begin during the earliest phases of protostellar evolution. Furthermore, the lack of a significant H II region implies there is insufficient ionized wind luminosity to drive the outflow, and its mechanical energy must be derived from other sources such as magnetic fields and/or the transfer of angular momentum from infalling material. Evidence that infall may be ongoing is found in the mean radial velocity of vibrational lines of gaseous CO at 4.7 μm (26 ± 2 km s^{-1}; Mitchell et al. 1990). These absorption lines probably arise in warm gas within ~ 50 AU of the photosphere of IRS 1 (Mitchell et al.; Paper I). The redshift by 4 km s^{-1} of this material relative to the systemic velocity of CRL 2136 ($V_{\rm LSR} = 22 \pm 1$ km s^{-1}; § 3.1) suggests it is infalling.

4.3. *Cloud Kinematics*

Since the outflow appears to blend smoothly into the larger-scale velocity structure of the molecular cloud (Fig. 6), it is difficult to separate outflow and cloud kinematics. Nonetheless, it appears that there is a significant component of shear or rotation in the molecular cloud containing CLR 2136 (§ 3.3). Significantly, the observed large-scale cloud velocities (Figs. 2*a* and 8) and estimated cloud masses may be consistent with pure Keplerian rotation around the CLR 2136 core (Table 3B), although our data are inconclusive on this point. Spectral line maps of ^{13}CO on large scales at higher velocity resolution would provide a test of the rotation hypothesis, although it may not be possible to construct a unique model of the cloud kinematics from such data. Data presented here appear to indicate, however, the profound affect of a massive protostellar core on the large-scale energetics of its host cloud.

5. CONCLUSIONS

Maps of ^{12}CO and ^{13}CO $J = 1 \rightarrow 0$ and $J = 2 \rightarrow 1$ emission reveal a parsec-scale bipolar outflow from the star formation region CRL 2136. The source of the outflow appears to be IRS 1, a massive young stellar object that illuminates a complex near-infrared reflection nebula. A large-field near-infrared image suggests that other, fainter stars within $\sim 1'$ of IRS 1 are mainly, and perhaps exclusively, background objects. The projected outflow axis lies perpendicular to the equatorial plane inferred from near-infrared polarization data (Paper I; Minchin et al. 1991). The outflow axis appears to be inclined out of the sky by $\lesssim 40°$, with the near lobe lying to the southeast and the far lobe to the northwest, and is closely aligned with two of the three principal near-infrared scattering lobes. In light of evidence that icy grains are confined to a circumstellar disk surrounding IRS 1 (Paper I), the moderate inclination of the outflow constrains the disk to be very thick or highly flared. The peaks of CS and ^{13}CO line emission and 800 μm continuum emission all lie a few arcsec southeast of IRS 1, suggesting the YSO lies $\sim 10{,}000$ AU from the cloud core. The outflow to the southeast may have bifurcated around this obstacle, producing the distinctive morphology of the near-infrared Juggler nebula.

Comparison of the intensities of ^{12}CO and ^{13}CO high-velocity emission indicates that the ^{12}CO optical depths are large ($\tau \sim 10$–20) and the gas excitation temperature is somewhat low (~ 5–10 K) for a molecular outflow from a YSO. As suggested in § 3.6, however, if the outflow is clumpy the optical depths in ^{13}CO may be larger and the gas temperature underestimated. After correcting for ^{12}CO optical depth, we estimate that the bipolar lobes contain $\sim 50\ M_\odot$ of molecular gas, and that the CRL 2136 core contains a significant concentration of ambient cloud material. The dust mass we deduce from the submillimeter continuum ($\sim 1\ M_\odot$ within $\sim 8''$ of IRS 1), which originates with grains heated to ~ 40–60 K by IRS 1, is roughly an order of magnitude larger than the scattering dust mass (Paper I). Comparison of the mass in high-velocity gas with these dust mass estimates suggests that the gas-to-dust mass ratio in the outflow is between 10 and 100. The latter value would require that most of the submillimeter emission arises from grains that reside in the ambient cloud and/or in the circumstellar disk surrounding IRS 1, although the morphology of the submillimeter emitting region suggests instead that this emission traces dust that is entrained in the outflow. The radial distribution of cloud mass within ~ 4 pc of IRS 1 and the large-scale velocity structure of the cloud may be consistent with Keplerian rotation around the CRL 2136 core, although we cannot construct a unique model of cloud kinematics from these data.

The dynamical timescale of the outflow is perhaps an order of magnitude greater than the age of IRS 1, suggesting that the outflow began at a very early stage in the evolution of IRS 1. The systemic velocity of CRL 2136 as derived from the millimeter-wave line data (22 ± 1 km s^{-1}) suggests that near-infrared absorption features of vibrational CO (Mitchell et al. 1991) arise in redshifted gas projected toward IRS 1; hence, infall toward IRS 1 may be ongoing.

J. H. K. wishes to acknowledge the staff of Haystack Observatory for their effort in upgrading the 37 m telescope and instrumentation to achieve 3 mm capability. Thierry Forveille of the Grenoble Astrophysics Group (GAG) provided assistance with the installation of GAG radio spectral line analysis software at Haystack. We thank Richard Barvainis for comments on the manuscript. J. H. K.'s research was supported by a fellowship funded jointly by M. I. T. and the Harvard-Smithsonian Center for Astrophysics.

REFERENCES

Allen, D. A., Hyland, A. R., Longmore, A. J., Caswell, J. J., Gross, W. M., & Haynes, R. F. 1977, ApJ, 217, 108
André, P., Ward-Thompson, D., & Barsony, M. 1993, ApJ, 406, 122
Barvainis, R. E., Ball, J. A., Ingalls, R. P., & Salah, J. E. 1993, PASP, 105, 1334
Cabrit, S., & Bertout, C. 1990, ApJ, 348, 503
Carbit, S., Goldsmith, P. F., & Snell, R. L. 1988, ApJ, 334, 196
Carpenter, J. M., Snell, R. L., Schloerb, F. P., & Skrutskie, M. F. 1993, ApJ, 407, 657
Cohen, R. J., Baart, E. E., & Jonas, J. L. 1988, MNRAS, 231, 205
Dame, T. M., et al. 1987, ApJ, 322, 706
Duncan, W. D., Robson, E. I., Ade, P. A. R., Griffin, M. J., & Sandell, G. 1990, MNRAS, 243, 126
Draine, B. T., & Lee, H. M. 1984, ApJ, 285, 89
Erickson, N. R., Goldsmith, P. F., Novak, G., Grosslein, R. M., Viscuso, P. J., Erickson, R. B., & Predmore, C. R. 1992, IEEE Trans. Microwave Theory Tech., 40, 1
Fukui, Y., et al. 1989, in ESO Workshop on Low-Mass Star Formation, ed. B. Reipurth (Munich: ESO), 95
Garden, R. P., Haysashi, M., Gatley, I., Hasegawa, T., & Kaifu, N. 1991, ApJ, 374, 540

Haslam, C. T. G. 1974, A&AS, 15, 333
Henning, Th., Pfau, W., & Altenhoff, W. J. 1990, A&A, 227, 542
Hildebrand, R. H. 1983, QJRAS, 24, 267
Kastner, J. H., Weintraub, D. A., & Aspin, C. 1992, ApJ, 389, 357 (Paper I)
Kurtz, S., Likkel, L., Kastner, J. H., & Weintraub, D. A. 1994, in preparation
Lebofsky, M. J., Kleinman, S. G., Rieke, G. H., & Low, F. J. 1976, ApJ, 206, L157
Minchin, N. R., Hough, J. H., Burton, M. G., & Yamashita, T. 1991, MNRAS, 251, 522
Mitchell, G. F., Maillard, J.-P., Allen, M., Beer, R., & Belcourt, K. 1990, ApJ, 363, 554
Mundy, L. G., Snell, R. L., Evans, N. J., Goldsmith, P. F., & Bally, J. 1986, ApJ, 306, 670
Meyers-Rice, B. A., & Lada, C. J. 1991, ApJ, 368, 445
Ney, E. P., & Merrill, K. M. 1980, AFGL-TR-80-0050
Plambeck, R. L., Snell, R. L., & Loren, R. B. 1983, ApJ, 266, 321
Price, S. D., & Murdock, T. L. 1983, AFGL-TR-83-0161
Russell, A. P. G., Bally, J., Padman, R., & Hills, R. E. 1992, ApJ, 387, 219
Sandell, G., & Weintraub, D. A. 1994, in preparation
Scoville, N. Z., Sargent, A. I., Sanders, D. B., Claussen, M. J., Masson, C. R., Lo, K. Y., & Phillips, T. G. 1986, ApJ, 303, 416
Snell, R. I., Mundy, L. G., Goldsmith, P. F., Evans, N. J., & Erickson, N. R. 1984a, ApJ, 276, 625
Snell, R. I., Scoville, N. C., Sanders, D. B., & Erickson, N. R. 1984b, ApJ, 284, 176
St. Clair, Dinger, A., Dickinson, D. F., Gottlieb, C. A., & Gottlieb, E. W. 1979, PASP, 91, 830
Willner, S., et al. 1982, ApJ, 253, 174.